AIAA JOURNAL
Vol. 43, No. 5, May 2005

Nonlinear Disturbance Evolution Across a Hypersonic Compression Corner

Hongwu Zhao*
University of Colorado, Boulder, Colorado 80309
and
Ponnampalam Balakumar†
NASA Langley Research Center, Hampton, Virginia 23681

The nonlinear evolution of the second-mode disturbance across a compression corner under the hypersonic flow condition is studied by spatial direct numerical simulation in this investigation. A fifth-order weighted essentially nonoscillating scheme is employed for this simulation. After the mean flow is obtained, the two- and three-dimensional mono- or random-frequency disturbances are added into the mean flow at the beginning of the computational domain. The nonlinear simulations show that two-dimensional disturbance will become saturated downstream of the separation region when its amplitude grows to a quite large value. For three-dimensional monofrequency disturbance evolution, with appropriate initial disturbance amplitude, the nonlinear interactions of the oblique disturbance will first happen at the beginning of the separation region, and some superharmonics will begin to appear in this region, but only downstream of the separation region do these harmonics begin to grow rapidly. Among all of these superharmonics, (0,2) mode shows the greatest growth rate and is responsible for oblique breakdown. With the presence of the two-dimensional primary disturbance, the oblique disturbances show the significant growth rate downstream of the separation region when the two-dimensional primary disturbance reaches the nonlinear saturation. Both mono- and random-frequency disturbance evolution show that the growth of three-dimensional disturbance as a result of secondary instability is responsible for the boundary-layer transition.

Nomenclature

C_v	=	specific heat at constant volume
e	=	internal energy
e_t	=	total energy
F	=	nondimensional disturbance frequency
F_{ji}, F_{vji}	=	inviscid and viscous flux
f	=	disturbance frequency
J	=	Jacobian matrix
k_T	=	heat-conductivity coefficient
M	=	Mach number
Pr	=	Prandtl number
p	=	pressure
$\boldsymbol{Q}$	=	conservative variable vector
R	=	gas constant
Re	=	Reynolds number
T	=	temperature
t	=	time
u_1, u_2, u_3	=	velocity in streamwise, wall normal, and spanwise directions
x_1, x_2, x_3	=	Cartesian coordinates
β	=	spanwise wave number
γ	=	specific heat constant
ε	=	initial disturbance amplitude
μ	=	viscosity coefficient
ν	=	kinematic viscosity
ξ, η, ζ	=	curvilinear coordinates
ρ	=	density
τ_{ij}	=	shear-stress tensor
ω	=	disturbance frequency

Subscripts

ref	=	reference variables
0	=	mean flow variables and initial streamwise location
∞	=	upstream infinity flow variables

Superscripts

$\hat{}$	=	numerical flux
-	=	variables in curvilinear coordinate system
$\sim$	=	normal mode variables

Introduction

IN this investigation, spatial direct numerical simulation is employed to study the nonlinear evolution of the second-mode disturbance in the hypersonic boundary layer across a compression corners. As we know, when a large adverse pressure gradient exists in the inviscid pressure distribution, the viscous effects become important. The interaction of the boundary layer and the pressure gradient modifies the pressure distribution, and the flowfield is drastically modified including multiple shocks, flow separation, transition to turbulence, unsteadiness, and three-dimensionality. These phenomena are observed in the experiments of transonic flow over airfoils by Ackert et al.[1] and supersonic flows over compression corners, bases, and steps by Chapman et al.[2] It can be seen from these experiments that the flow separates some distance upstream of the shock impingement point and a separation bubble forms across the shock on the wall surface. And the transition location has a significant influence on the pressure distribution along the wall surface.

In general, transition arising from a separated region of flow is quite common and plays an important role in engineering. But it is difficult to predict using conventional models, and transition mechanism is still not fully understood. Transition mechanism in the separation bubble for incompressible flow was studied by Spalart and Strelets[3] using large-eddy simulation and also by Yang and Voke[4] using direct numerical simulation. Their results show that the instability mechanism in the separation bubble for incompressible flow is dominated by Kelvin–Helmholtz instability. With large adverse-pressure-gradient existence, the boundary layer in the separation

Received 4 May 2003; revision received 22 October 2003; accepted for publication 2 November 2004.

*Research Associate, Department of Aerospace Engineering Science. Member AIAA.
†Aerospace Engineer, Flow Physics and Control Branch. Member AIAA.

bubble is thought to be inviscid unstable. More recently, Balakumar et al.[5] studied the stability of hypersonic boundary layer over a compression corner by direct numerical simulation. Their results showed the linear evolution of the two-dimensional second-mode disturbance across a compression corner and demonstrated a different instability mechanism in the separation bubble region for compressible flow. According to their results, the boundary layer in the separation region is relatively more stable in hypersonic flow than in incompressible flow.

However, a lot of experimental and numerical work had actually shown the three-dimensional nature of the transition. The classical experiment made by Klebanoff et al.[6] had demonstrated that the actual breakdown of the wave motion into turbulence is a consequence of a new instability that arises in the aforementioned three-dimensional wave motion. This instability involves the generation of staggered Λ vortices, and the transition begins at the peak planes. Pruett et al.[7] and Pruett and Chang[8] performed a spatial direct numerical simulation of transition on a cone in Mach 8 flow. Their results show that oblique second-mode breakdown is a viable path to transition for a high-speed boundary-layer flow on a cone. They also demonstrate that the (0,2) mode which arises primarily from the nonlinear interactions of the oblique second-mode waves present in the initial disturbance eventually dominates all other harmonics and is believed to be responsible for the oblique breakdown. So in order to understand the transition mechanism of the hypersonic boundary layer across the compression corner, it is necessary to study the oblique disturbance evolution across the compression corner. The objective of current study is to study the nonlinear evolution of both two- and three-dimensional second-mode disturbances across a compression corner. The nonlinear mode interaction and the growth of the superharmonics will be investigated in all three flow regions.

To compute the shock and the interaction of the shock with boundary layer, the two-dimensional Navier–Stokes (N-S) equations were solved using a fifth-order weighted essentially nonoscillating (WENO) shock-capturing scheme. After the mean flowfield is computed, unsteady two- and three-dimensional disturbances are introduced at the upstream end of the computational domain, and time-accurate computations are performed. The first section of this paper presents the governing equations. This is followed by a brief description of the numerical method used to solve the three-dimensional N-S equations. Finally, the results are presented.

Governing Equation

The equations solved are the three-dimensional unsteady compressible Navier–Stokes equations in conservation form:

$$\frac{\partial}{\partial t}(\boldsymbol{Q}_i)+\frac{\partial}{\partial x_j}(F_{ji}-F_{vji})=0, \qquad i=1\cdots 3, \qquad j=1\cdots 3 \tag{1}$$

$$\boldsymbol{Q}_i=[\rho,\rho e_t,\rho u_1,\rho u_2,\rho u_3]^T \tag{2}$$

$$F_{ji}=[\rho u_j,(\rho e_t+p)u_j,\rho u_1u_j+\delta_{1j}p,\rho u_2u_j+\delta_{2j}p,\rho u_3u_j+\delta_{3j}p]^T \tag{3}$$

$$F_{vji}=[0,u_1\tau_{1j}+u_2\tau_{2j}+u_3\tau_{3j}-q_j,\tau_{1j},\tau_{2j},\tau_{3j}]^T \tag{4}$$

where

$$e_t=e+\frac{u^2+v^2+w^2}{2}, \qquad e=c_vT, \qquad p=\rho RT \tag{5}$$

$$\tau_{ij}=\mu\left[\frac{\partial u_i}{\partial x_j}+\frac{\partial u_j}{\partial x_i}-\frac{2}{3}\delta_{ij}\frac{\partial u_k}{\partial x_k}\right], \qquad q_j=-k\frac{\partial T}{\partial x_j} \tag{6}$$

The viscosity μ is computed using Sutherland's law, and the coefficient of conductivity k_T is given in terms of the Prandtl number Pr. The variables ρ, p, T, and velocity are nondimensionalized by their corresponding reference variables ρ_∞, p_∞, T_∞, and $\sqrt{RT_\infty}$, respectively. The reference value for length is computed by $\sqrt{\nu x_0/U_\infty}$, where x_0 is the location of the beginning of computational domain in streamwise direction. For the convenience of computation, the equation are transformed from physical coordinate system (x, y, z) to the computational coordinate system (ξ, η, ς) in a conservative manner such that the general form of the equations is unchanged:

$$\frac{\partial}{\partial t}(\bar{\boldsymbol{Q}}_i)+\frac{\partial}{\partial \xi_j}(\bar{F}_{ji}-\bar{F}_{vji})=0, \qquad i=1\cdots 3, \qquad j=1\cdots 3 \tag{7}$$

The components of the flux in the computational domain are related to the flux in the Cartesian domain by

$$[\bar{\boldsymbol{Q}}_i]=[\boldsymbol{Q}_{ji}]/|J|, \qquad [\bar{F}_{ji}]=(J/|J|)[F_{ji}]$$

$$[\bar{F}_{vji}]=(J/|J|)[F_{vji}] \tag{8}$$

where

$$J=\left[\frac{\partial(\xi,\eta,\varsigma)}{\partial(x,y,z)}\right]$$

Solution Algorithm

The governing equations are solved using the fifth-order-accurate WENO scheme for space discretization and using third-order total-variation-diminishing (TVD) Runge–Kutta scheme for time integration. The WENO scheme and TVD methods are explained in Shu,[9] and application of ENO method to N-S equations is given in Atkins.[10] The governing equations are solved discretely in a uniform structured computational domain in which flow properties are known pointwise at the grid nodes. The spatial derivatives in a given direction are approximated to higher order at the nodes using the neighboring nodal values in that direction, and the resulting equations are integrated in time to get the point values as a function of time. Because the spatial derivatives are independent of the coordinate directions, multidimensions can easily be added into the method. It is well known that approximating a discontinuous function by a higher-order (two or more) polynomial generally introduces oscillatory behavior near the discontinuity and this oscillation increase with the order of the approximation. The ENO and the improvement of these WENO methods are developed to keep the higher-order approximations in the smooth regions and to eliminate or suppress the oscillatory behavior near the discontinuities. They are achieved by systematically adopting or selecting the stencils based on the smoothness of the function, which is being approximated.

Consider the equation

$$\frac{\partial \bar{\boldsymbol{Q}}}{\partial t}+\frac{\partial \bar{F}}{\partial \xi}=0 \tag{9}$$

The kth-order conservative approximation to the spatial derivative is written as

$$\frac{\partial \bar{F}}{\partial \xi}(\xi_i)=\frac{\hat{F}\left(\xi_{i+\frac{1}{2}}\right)-\hat{F}\left(\xi_{i-\frac{1}{2}}\right)}{\Delta\xi}+\mathcal{O}(\Delta\xi^k), \qquad i=0,1,\ldots,N \tag{10}$$

Here the numerical flux $\hat{F}$ is determined from the linear combination of the flux values at the neighboring nodes

$$\hat{F}^{(r)}\left(\xi_{i+\frac{1}{2}}\right)=\sum_{j=0}^{k-1}c_{rj}\bar{F}(\xi_{i-r+j}), \qquad r=0,1,\ldots,k-1 \tag{11}$$

and the coefficients c_{rj} are determined from the Taylor-series expansion. As it is seen, the value of r is left open, and the choice of r will determine the stencil used to determine the spatial derivative at the point ξ_i. This is the basic strategy behind the ENO scheme. The value of r is determined using the function values $\bar{F}(\xi_i)$ and the Newton divided differences. Out of possible k stencils, the ENO method picks up only one stencil to give uniformly high order up to the discontinuity. However, the selection of stencils is very sensitive to the function values $\bar{F}(\xi_i)$, and the WENO scheme is developed to improve the ENO scheme.

In the WENO scheme instead of selecting one stencil, first the numerical flux from all of the possible stencils are computed, and

they are combined to obtain the numerical flux

$$\hat{F}\left(\xi_{i+\frac{1}{2}}\right) = \sum_{r=0}^{k-1} \omega_r \hat{F}^{(r)}\left(\xi_{x+\frac{1}{2}}\right) = \bar{F}\left(\xi_{i+\frac{1}{2}}\right) + \mathcal{O}(\Delta\xi^{2k-1}) \quad (12)$$

The weight function ω_r is selected to get $2k-1$ order accuracy in the smooth regions and to give order k accuracy near the discontinuity as in the ENO scheme. In the smooth regions one can find coefficients such that

$$\hat{F}\left(\xi_{i+\frac{1}{2}}\right) = \sum_{r=0}^{k-1} d_r \hat{F}^{(r)}\left(\xi_{x+\frac{1}{2}}\right) = \sum_{j=0}^{2k-1} c_{rj} \hat{F}\left(\xi_{x-r+j}\right), \qquad r = r_0 \quad (13)$$

For $k=3$, d_r are given by

$$d_0 = 3/10, \qquad d_1 = 3/5, \qquad d_2 = 1/10 \quad (14)$$

and this gives upwind-biased fifth-order accuracy for the derivative on a six-point stencil. Near nonsmooth regions, the weights are made to become zero for the stencils that contain the discontinuity, and this is achieved by selecting the weights ω_r in the following form:

$$\omega_r = \frac{\alpha_r}{\sum_{s=0}^{k-1} \alpha_s}, \qquad r = 0, \ldots, k-1 \quad (15)$$

$$\alpha_r = \frac{d_r}{(\varepsilon_0 + \beta_r)^2} \quad (16)$$

Here $\varepsilon_0 > 0$ is introduced to avoid the denominator to become 0. And β_r is the smooth indicator for rth interpolation stencil. It was determined by the undivided differences of density at the reference point ξ_i. For $k=3$, we have

$$\beta_0 = (13/12)(\rho_i - 2\rho_{i+1} + \rho_{i+2})^2 + \tfrac{1}{4}(3\rho_i - 4\rho_{i+1} + \rho_{i+2})^2 \quad (17)$$

$$\beta_1 = (13/12)(\rho_{i-1} - 2\rho_i + \rho_{i+1})^2 + \tfrac{1}{4}(\rho_{i-1} + \rho_{i+1})^2 \quad (18)$$

$$\beta_0 = (13/12)(\rho_{i-2} - 2\rho_{i-1} + \rho_i)^2 + \tfrac{1}{4}(\rho_{i-2} - 4\rho_{i-1} + 3\rho_i)^2 \quad (19)$$

The flux splitting is performed to the inviscid flux terms based on their characteristic values. We used the simple Lax–Friedrichs flux splitting in the form

$$\bar{F}_k = \bar{F}_k^+ + \bar{F}_k^- \quad (20)$$

$$\bar{F}_k^{\mp} = \bar{F}_k \mp \lambda \bar{\boldsymbol{Q}} \quad (21)$$

and λ is taken as the maximum eigenvalue of the Jacobian matrix.

With the spatial operator treated as a forcing term, the time integration is performed using the third-order TVD Runge–Kutta method

$$\bar{\boldsymbol{Q}}^{(1)} = \bar{\boldsymbol{Q}}^n + \Delta t L(\bar{\boldsymbol{Q}}^n) \quad (22)$$

$$\bar{\boldsymbol{Q}}^{(2)} = \tfrac{3}{4}\bar{\boldsymbol{Q}}^n + \tfrac{1}{4}\bar{\boldsymbol{Q}}^{(1)} + \tfrac{1}{4}\Delta t L\left(\bar{\boldsymbol{Q}}^{(1)}\right) \quad (23)$$

$$\bar{\boldsymbol{Q}}^{n+1} = \tfrac{1}{3}\bar{\boldsymbol{Q}}^n + \tfrac{2}{3}\bar{\boldsymbol{Q}}^{(2)} + \tfrac{2}{3}\Delta t L\left(\bar{\boldsymbol{Q}}^{(2)}\right) \quad (24)$$

where $L(\bar{\boldsymbol{Q}})$ is an WENO approximation to the spatial derivative of flux vector $\bar{\boldsymbol{F}}$. And the time step is determined on the basis of an inviscid Courant–Friedrichs–Lewy (CFL) number,

$$\mathrm{CFL} = \frac{\Delta t}{|J|} \sum_{k=1}^{3} |\lambda_k| \quad (25)$$

where λ_k are the eigenvalues of the Jacobian matrix.

The procedure is to first compute the steady mean flow. This is achieved by performing unsteady computations using variable time step until the residual reaches a small value $\sim 10^{-5}$. We used a CFL number of 0.6. To investigate the evolution of instability waves, unsteady disturbances are introduced at the upstream end of the computational domain, and time-accurate computations are performed. The disturbances are added into the mean flow according to the following equations:

$$q(x_0, y, z, t) = \boldsymbol{Q}_0(x_0, y) + \varepsilon Real[\tilde{q}(y)\exp(i\beta z - i\omega t) + \exp(-i\beta z - i\omega t)] \quad (26)$$

$$q(x_0, y, z, t) = \boldsymbol{Q}_0(x_0, y) + \varepsilon_{2D} Real[\tilde{q}(y) e^{-i\omega t}] + \varepsilon_{3D} \sum_n \sum_m Real[\tilde{q}_{\mathrm{nm}}(y)\exp(i\beta_m z - i\omega_n t) + \exp(-i\beta_m z - i\omega_n t)] \quad (27)$$

$$\boldsymbol{q} = [\rho, e_t, u, v, w]^T, \qquad \boldsymbol{Q}_0 = [\rho_0, Et_0, U_0, V_0, W_0]^T$$

$$\tilde{q} = [\tilde{\rho}, \tilde{e}_t, \tilde{u}, \tilde{v}, \tilde{w}]^T \quad (28)$$

ε_{2D} and ε_{3D} are the initial disturbance amplitudes for two-dimensional primary disturbances and three-dimensional random disturbances, respectively; $\tilde{q}$ is the eigenfunction that is obtained by the parabolic stability equation method; $\boldsymbol{Q}_0$ is the steady mean flow profiles at the initial streamwise location; and x_0 is the coordinate of the initial streamwise location.

In Eq. (26), only the monofrequency three-dimensional disturbance are introduced, and in Eq. (27) both three-dimensional random-frequency disturbance and two-dimensional primary disturbance are introduced. The random-frequency disturbances are introduced by adding the white noise.

Geometry of the Model, Flow Parameters, and Computational Grid

The computations are performed across a 5.5-deg compression corner under the hypersonic flow condition. The geometry of the computational model is illustrated in Fig. 1. It is a Hyper-X model with two corners; the computation in present study only focuses on the disturbance evolutions across the first corner. The flow parameters are given in Table 1. These parameters are selected to simulate the Hyper-X wind-tunnel model and the experimental conditions. Figure 2 shows the computational grid. The grid is generated using analytical conformal mapping formulas and is stretched in Y direction close to the wall. The grid size is $1701 \times 301 \times 30$ in X, Y, and Z direction respectively. Because of the slow computational speed and big memory needed for such big grid, in this study a message-passing-interface parallel algorithm was adopted in this code so that it can be run on multiprocessors. where the nondimensional frequency F is expressed as $F = 2\pi\nu_\infty f/U_{\mathrm{ref}}^2$.

Table 1 Flow parameters

Parameter	Value
Freestream Mach number M_∞	5.373
Freestream Reynolds number Re_∞	5.464×10^6/ft (1.665×10^6/m)
Freestream density ρ_∞	6.0891×10^{-3} lbm/ft^3 (9.7538×10^2 kg/m^3)
Freestream pressure p_∞	43.384 lbf/ft^2 (2077.2259 N/m^2)
Freestream velocity U_∞	3043.86 ft/s (927.7685 m/s)
Reference velocity U_{ref}	478.79 ft/s (145.9352 m/s)
Freestream temperature T_∞	133.55°R (74.1945 K)
Freestream kinematic viscosity	5.5707×10^{-4} ft^2/s (5.1753×10^{-5} m^2/s)
Wall temperature T_{wall}	540°R (300 K)
Prandtl number Pr	0.72
Ratio of specific heats γ	1.4
Nondimensional frequency $F = 1.0 \times 10^{-4}$	264.7 kHz

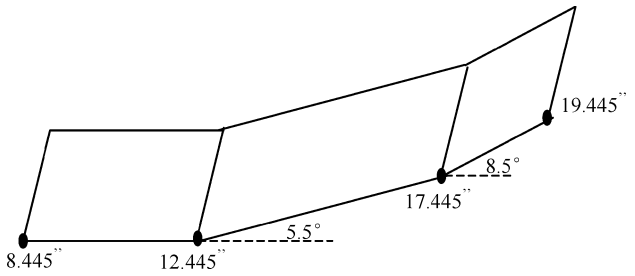

Fig. 1 Geometry of compression corner.

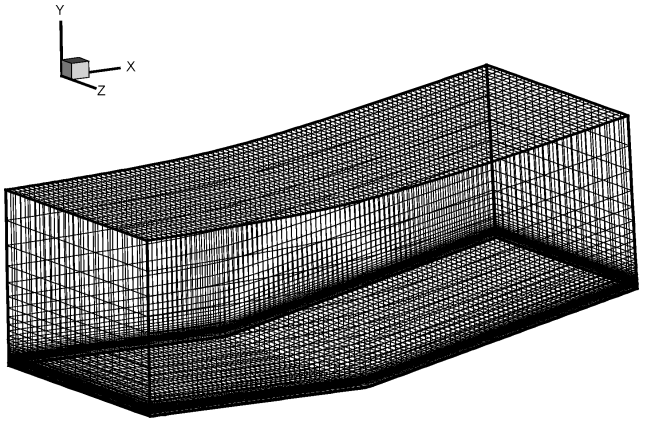

Fig. 2 Computational grid.

Results and Discussion

In the simulation of the nonlinear disturbance evolution, we chose a dimensionless primary disturbance frequency $F = 0.85 \times 10^{-4}$ because based on the linear stability computation results given in Balakumar et al.[5] this frequency located inside the second-mode unstable region and both two- and three-dimensional disturbances are amplified significantly across the compression corner at this frequency. The spanwise wave number is also chosen based on the linear stability computation results so that the three-dimensional disturbance can keep a big growth rate across the compression corner. In addition, because we are going to show the nonlinear disturbance evolution across the separation region as well as downstream of the separation region, the initial disturbance amplitude should be chosen according to the criteria that the flow will not transit to turbulence upstream of the separation region, and disturbances can reach the nonlinear interaction inside the separation region. To fully understand the transition mechanism, several computational cases are presented in the following discussion:

1) Mean flow computation results is the first case. In this study, the mean flow is two-dimensional boundary-layer flow across the compression corner, which have been obtained by Balakumar et al.[5] Figure 3 shows the mean flow density contours, and Fig. 4 shows the mean flow streamline patterns. It is shown that the flow separates across the compression corner and a separation bubble forms at the corner point. The separation location is at $x = 10.8$ in., and reattachment location is at $x = 14.1$ in.

2) The nonlinear evolution of two-dimensional disturbance across the compression corner is the next case.

Figure 5 shows the nonlinear evolution of two-dimensional density disturbance at frequency $F = 0.85 \times 10^{-4}$ and initial disturbance amplitude $\varepsilon = 0.01$. It is observed that the disturbance grows upstream of the separation and remains approximately neutral inside the separation region. Downstream of the separation region, the disturbance first shows significant growth tendency, and this growth tendency decreases gradually further downstream. Finally, the disturbance stops growing and becomes saturated when its amplitude reaches about 60% of its upstream infinity mean density value. If we decompose this density disturbance by discrete Fourier transformation, we can obtain the evolution of different harmonic modes across the compression corner shown as Fig. 6. It is observed that harmonics

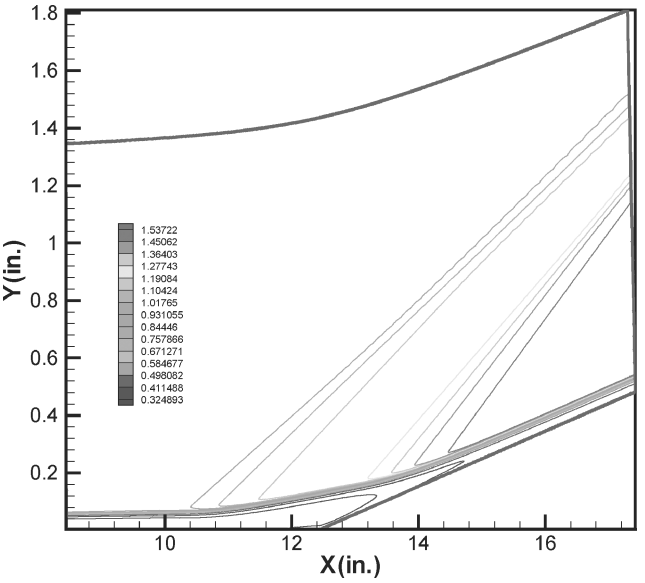

Fig. 3 Mean flow density contour.

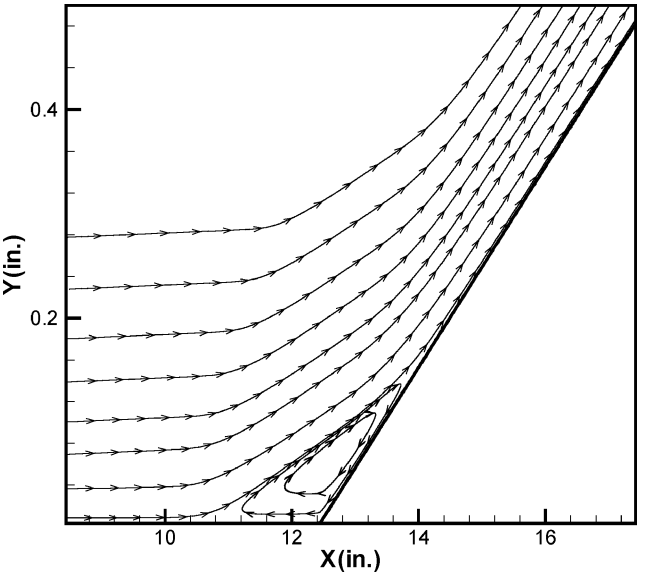

Fig. 4 Mean flow streamline pattern.

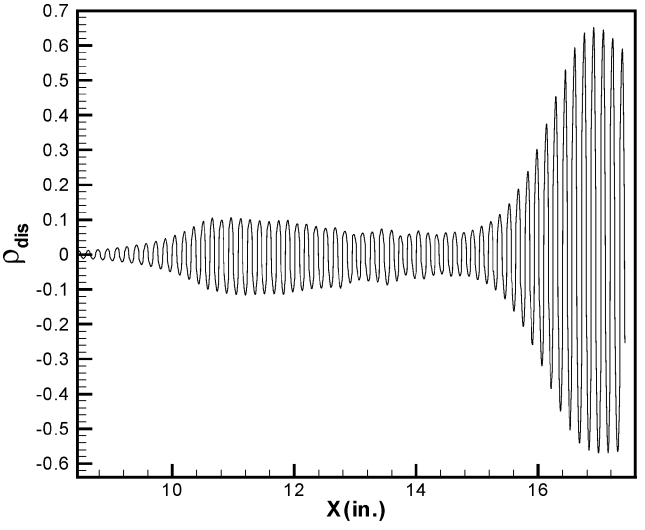

Fig. 5 Maximal density disturbance for two-dimensional nonlinear disturbance evolution.

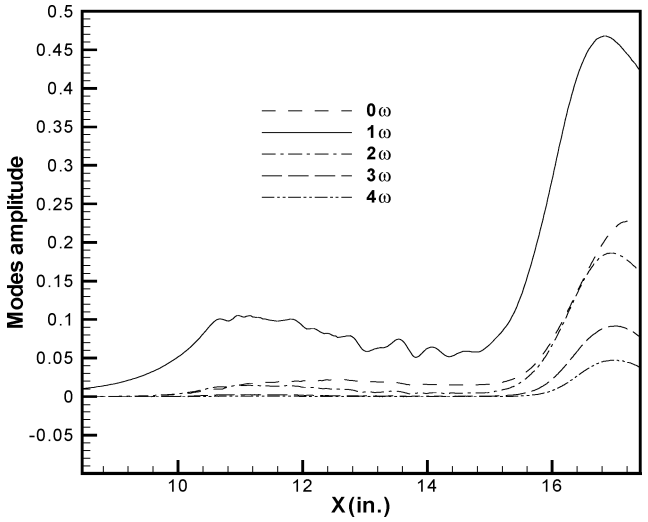

Fig. 6 DFT analysis results for two-dimensional maximal density disturbance.

caused by nonlinear interaction begin to appear in the separation region, and they only show significant growth rate downstream of the separation region. Among all of these harmonic modes, 1 ω represents the fundamental mode that is added into the mean flow at the initial location. 0 ω represents the mean flow distortion. And all other modes are superharmonic modes. We also notice that after the saturation of the fundamental mode, all other harmonic modes will also saturate regardless of its amplitude.

3) The nonlinear evolution of three-dimensional monofrequency disturbance without the presence of two-dimensional primary disturbance is the third case.

Figures 7–9 show the results of three-dimensional monofrequency disturbance evolution at the disturbance frequency $F = 0.85 \times 10^{-4}$, spanwise wave number $\beta = 0.1$, and initial disturbance amplitude $\varepsilon = 0.01$. Figure 7 shows the density disturbance contours in Y-Z planes at three streamwise locations $X = 8.445$, 12.984, and 16.545 in., respectively. These three locations belong to upstream of, inside, and downstream of the separation region, respectively. The contours are shown in one cycle in the spanwise direction. Upstream of the separation region, the disturbance amplitudes are still small, and the nonlinear effects can be negligible, and so the disturbances show the fundamental pure harmonic pattern in the spanwise

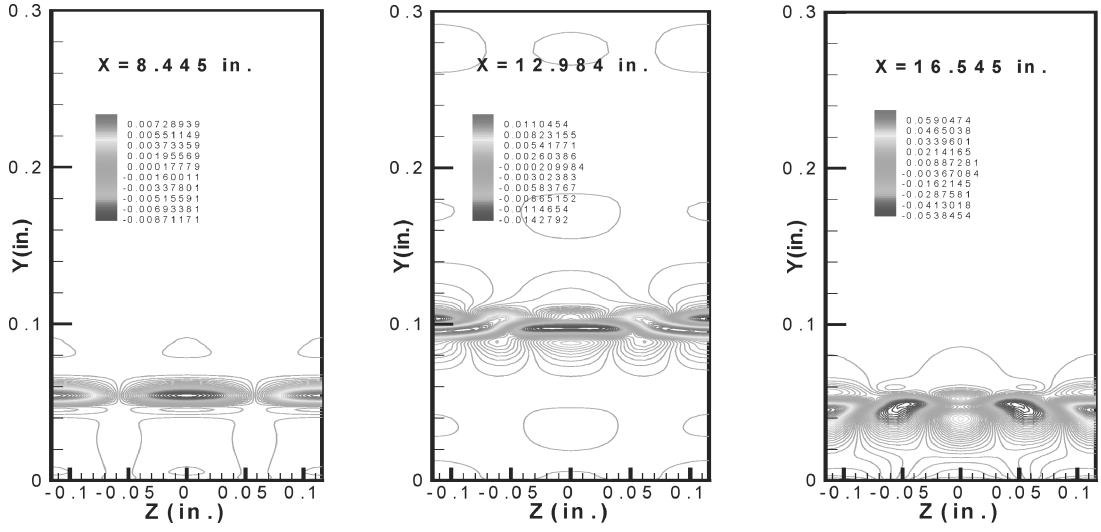

Fig. 7 Density disturbance contours in Y-Z planes at different streamwise locations.

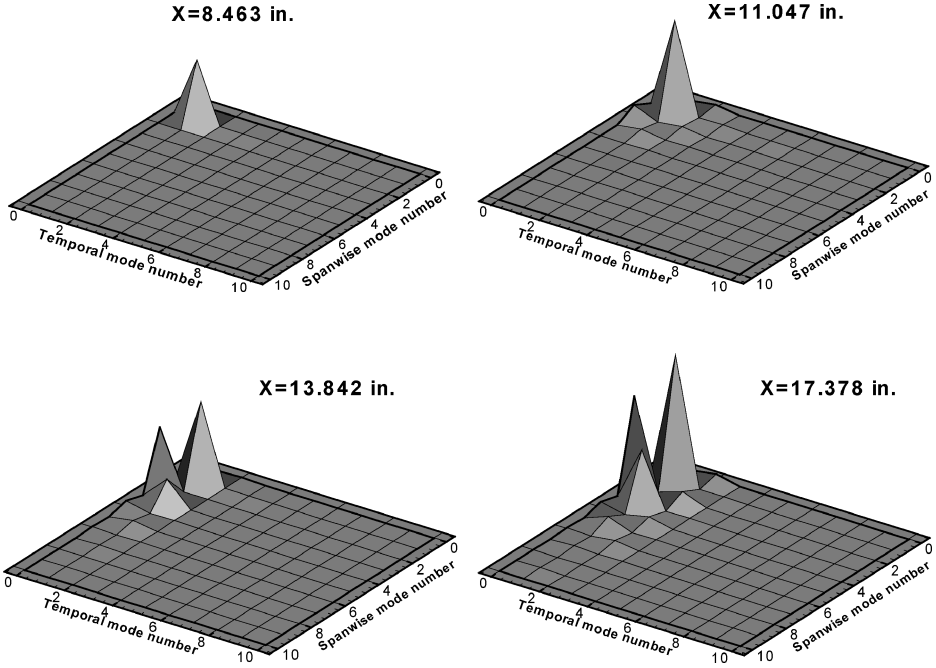

Fig. 8 Spectral distributions of the density disturbances at different streamwise locations.

direction. Inside the separation region, the weak nonlinear interaction begins to appear. Compared with the contours at $X = 8.445$ in., the contours at $X = 12.984$ in. begin to show some distortions from the fundamental pure harmonic patterns. Downstream of the separation region, the nonlinear interactions become much stronger. With more and more harmonics added into the primary disturbance, the contours show much more complicated patterns.

To show which harmonics have appeared during the nonlinear interaction, we take the data in one cycle of both time and in the spanwise direction and perform the two-dimensional discrete Fourier transformation (DFT) to decompose the total disturbance into harmonic modes $(m\omega, n\beta)$, where m, n stand for the mode numbers for frequency and spanwise wave number, respectively. Figure 8 shows the Fourier-mode distributions for density disturbance at different streamwise locations. Each mode is shown in its maximal amplitude in the normal direction. It is observed that at $X = 8.643$ in. the nonlinear effects are very small, so that only the primary mode (1,1) is present at this location. At $X = 11.047$ in., which is located at the beginning of the separation region, the nonlinear interactions begin to take effect at this location, so that the superharmonics begin to appear. At the location $X = 13.842$ in., which is located close to the end of the separation region, the nonlinear interactions become strong, and more harmonics appear. At the location $X = 17.378$ in., which is located close to the end of the downstream of the separation region, the nonlinear interactions become much stronger, and some harmonics such as (0,2) and (1,3) modes have reached the amplitudes that are comparable to that of the primary disturbance.

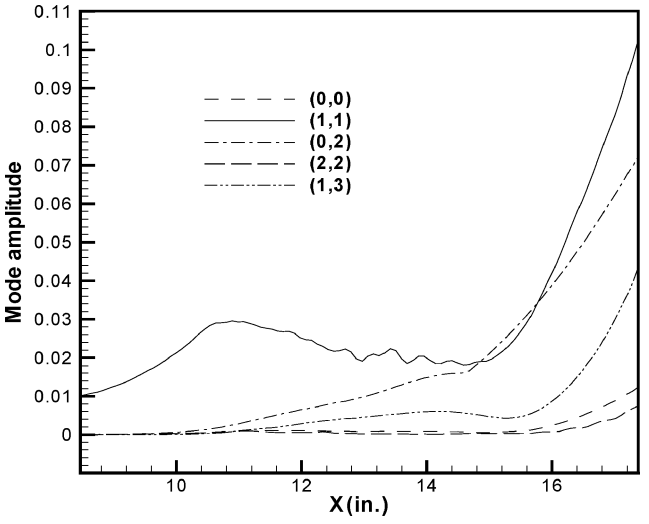

Fig. 9 Streamwise amplitude distributions of different modes for density disturbance.

Figure 9 shows the maximal amplitude distributions in the streamwise direction for those Fourier modes whose amplitudes can exceed 0.001. It can be seen that the primary mode (1,1) dominates in most parts of the streamwise region. Among all superharmonic modes produced by nonlinear interactions, the mode (0,2) shows a very distinct characteristic. It grows in the separation region and reaches a very large amplitude in both the separation region and downstream of the separation region. It even surpasses the primary mode in the region close to the reattachment point. This mode is believed to be responsible for the oblique breakdown.

4) The nonlinear evolution of three-dimensional monofrequency disturbance in the presence of the two-dimensional primary disturbance is the fourth case.

As we know, most transitions are caused by the growth of three-dimensional waves by secondary instabilities; in the present study, another computational case was performed to study the three-dimensional instability across the compression corner in the presence of the two-dimensional instability wave. To perform this simulation, a two-dimensional second mode and an oblique mode were introduced at the initial streamwise location. Both the two-dimensional and oblique modes possess the same frequency $F_0 = 0.85 \times 10^{-4}$. The spanwise wave number for the oblique mode was $\beta = 0.1$. The initial amplitude of the two-dimensional mode is $\varepsilon_{2D} = 0.005$, and the initial amplitude of the oblique mode was $\varepsilon_{3D} = 0.001$.

Figure 10 shows the spectral distributions of the density disturbance at different streamwise locations. It is observed that at the streamwise location $X = 8.463$ in. upstream of the separation region, only the fundamental two-dimensional mode (1,0) and oblique mode (1,1) are present. At the locations $X = 11.951$ in., which is in the separation region, the two-dimensional mode has grown to a quite large amplitude. But the oblique mode shows very little growth, and no other harmonics appear in this region. The superharmonics begin to appear downstream of the separation region. At the location $X = 17.378$ in., which is close to the end of the computational domain, many of harmonic modes have already been observed to form a continuous spectrum distribution of disturbances. Figures 11 and 12 show the spanwise vortex distributions

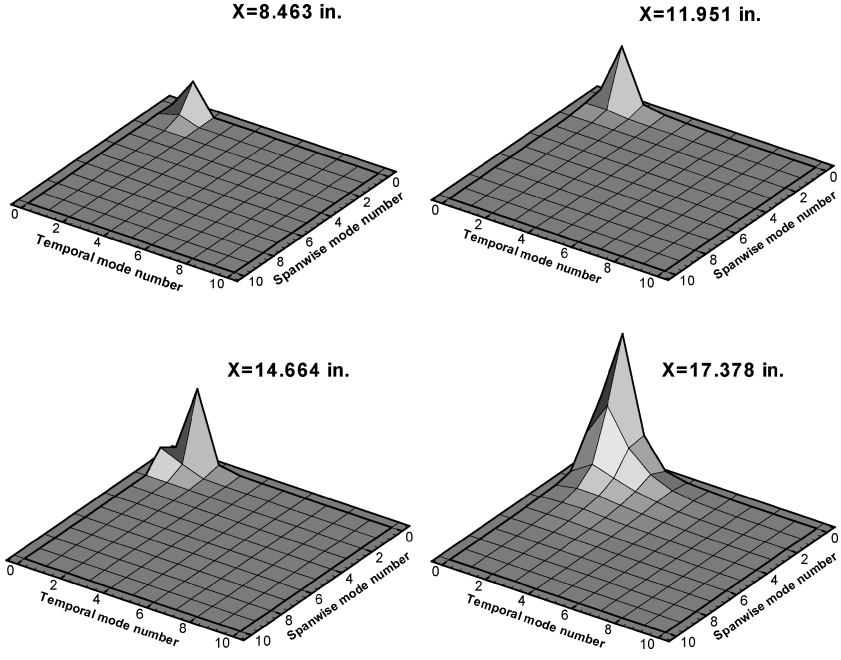

Fig. 10 Spectral distributions of the disturbances at different streamwise locations.

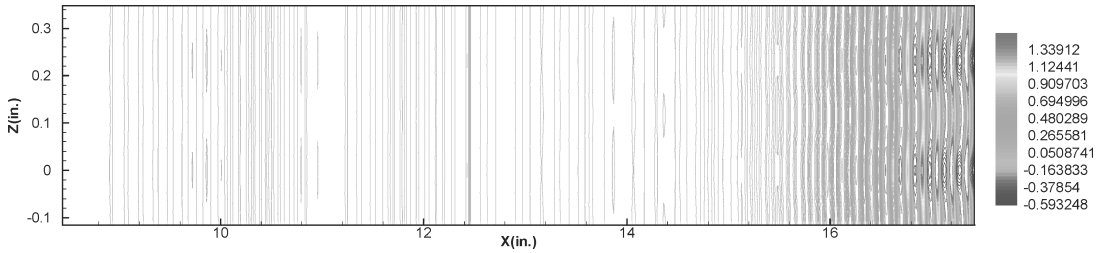

Fig. 11 Spanwise vortices distributions on the wall.

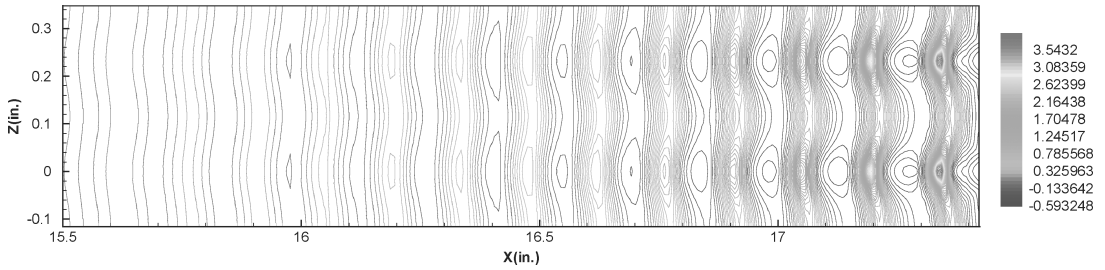

Fig. 12 Expanded view of spanwise vortices distribution downstream of the separation.

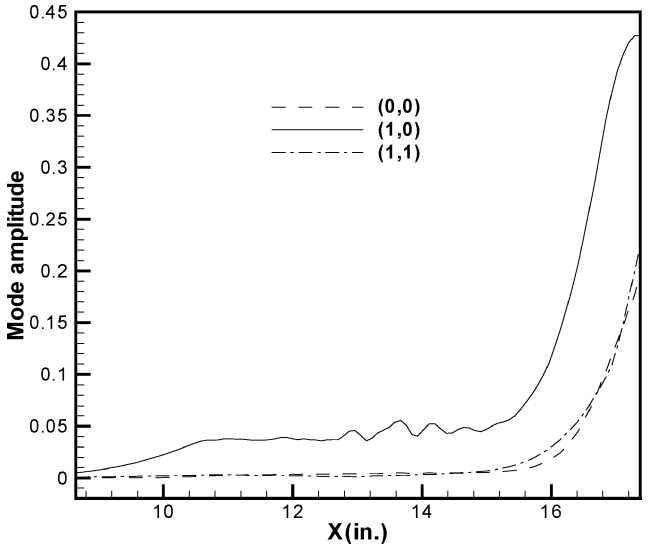

Fig. 13 Streamwise amplitude distributions for different Fourier modes.

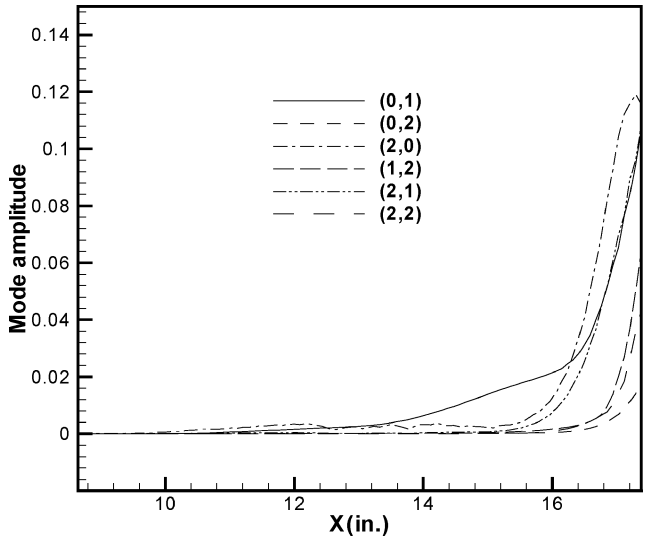

Fig. 14 Streamwise amplitude distributions for different Fourier modes.

on the wall. It is observed that upstream of and inside the separation region the instability vortices possess two-dimensional characteristics, but downstream of the separation region the instability vortices begin to exhibit three-dimensional characteristics. The three-dimensional instability vortices grow continuously farther downstream. We also noticed that the three-dimensional vortices showed an alignment pattern in the spanwise direction. So the growth of the three-dimensional instability vortices will lead to the fundamental laminar breakdown.

Figures 13 and 14 show the amplitude distributions for each Fourier mode whose amplitude had reached a quite large value downstream of the separation region. It is observed that the two-dimensional fundamental mode (1,0) shows the same nonlinear growing characteristics as that computed when no oblique mode is present. It grows upstream and downstream of the separation region, remains neutral in the separation region, and begins to saturate near the end of the computational domain. But for the three-dimensional fundamental oblique mode, little growth can be observed upstream of as well as inside the separation region. However, it shows a significant growth downstream of the separation region. Compared with the growth of the three-dimensional mode without the presence of the two-dimensional mode, the growth of the three-dimensional mode with the presence of the two-dimensional mode downstream of the separation region is remarkable. The growth rate for the former case is only 20 times, but the growth rate for the later case can reach almost 200 times. This three-dimensional mode will continue to grow when the two-dimensional mode begins to saturate until it reaches the same amplitude as that of the two-dimensional mode.

It can also be observed in Figs. 13 and 14 that the harmonics caused by the nonlinear interactions begin to appear in the separation region. However, only downstream of the separation region do these harmonics show significant growth rate. Among them, the (0,0) mode that shows the distortion of the mean flow just follows the growth of the fundamental modes (1,0) and (1,1). All other harmonics grow independently. An interesting observation is that all three-dimensional harmonics will grow continuously when the two-dimensional fundamental mode begins to saturate. All two-dimensional harmonics will also saturate with the saturation of the two-dimensional fundamental mode. We also notice that the (0,1) mode, which is basically the stationary longitudinal vortex mode, shows a remarkable growth characteristic. It grows in the separation region and surpasses all other harmonics in amplitude at the end of the separation region. Downstream of the separation region, it again shows significant growth rate as a result of the secondary instability. This mode also plays a very important role in laminar breakdown.

5) Three-dimensional random-frequency disturbance evolution in the presence of the two-dimensional primary disturbance is the last case.

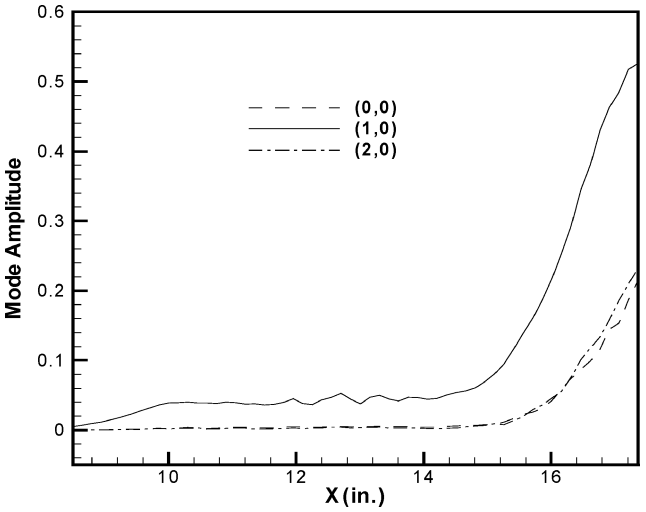

Fig. 15 Streamwise amplitude distributions of three-dimensional Fourier modes.

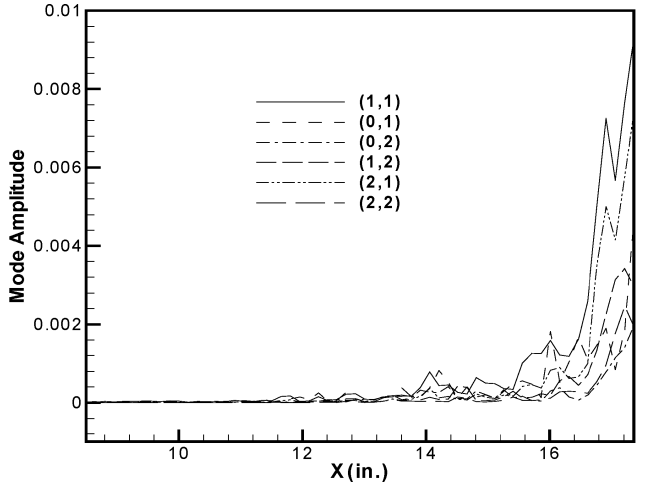

Fig. 16 Streamwise amplitude distributions of three-dimensional Fourier modes.

In this paper, we also study the three-dimensional random-frequency disturbance evolutions across the compression corner in the presence of the two-dimensional primary disturbance. The primary disturbance frequency is $F = 0.85 \times 10^{-4}$. The initial disturbance amplitude for two-dimensional primary disturbance is $\varepsilon_{2D} = 0.005$ and for three-dimensional random disturbances is $\varepsilon_{3D} = 0.0001$. Because of these three-dimensional random disturbances, which are added at the initial streamwise location, now the second instability will select the most unstable three-dimensional disturbance frequency automatically. Figure 15 shows the streamwise amplitude distributions for two-dimensional primary disturbances and the other two-dimensional harmonics, which are produced by nonlinear interactions. It is observed that the two-dimensional primary disturbance and its harmonics show the same growth characteristics as those computed when no oblique mode is present. They saturate at the end of the streamwise computational domain. Figure 16 shows the three-dimensional disturbance evolution in the streamwise direction. It is observed that the three-dimensional disturbances are very small and almost neutral upstream of and inside the separation region where the two-dimensional primary disturbance amplitude is still small. However, when the three-dimensional disturbances reach downstream of the separation region, with the associated rapid increase of the two-dimensional primary amplitude, they also begin to grow rapidly. When the two-dimensional primary disturbance reaches saturation, the three-dimensional disturbances show a very significant growth rate as a result of the secondary instability. Among all of the three-dimensional harmonics, the (1,1) mode shows the largest growth rate. All of these three-dimensional disturbances will grow continuously further downstream to form the Λ vortices and lead to laminar breakdown.

Conclusions

Several conclusions can be obtained according to present numerical simulations. The simulations show that across the hypersonic compression corner nonlinear two-dimensional disturbance becomes saturated downstream of the separation region when its amplitude grows to a quite large value. For three-dimensional nonlinear monofrequency disturbance evolutions, the superharmonics begin to appear in the separation region, but only downstream of the separation region do most of these harmonics show an apparent growing tendency. Among all of these modes, mode (0,2) shows the characteristics of a stationary longitudinal vortex and has its biggest growth rate downstream of the separation region. This mode is responsible for the oblique breakdown. With the presence of the two-dimensional primary mode, the three-dimensional modes show much greater growth rates as a result of the secondary instability when the two-dimensional fundamental mode saturates. More and more harmonics begin to appear as a result of the secondary instability. Among these harmonics, all three-dimensional harmonics grow continuously, and all two-dimensional harmonics saturate with the saturation of the two-dimensional primary mode. The simulations of the three-dimensional random frequency disturbance evolutions in the presence of the two-dimensional primary disturbance show that the secondary instability begins to take effect downstream of the separation region. The three-dimensional disturbances will grow rapidly as a result of the secondary instability and finally leads to the laminar breakdown.

References

[1]Ackeret, J., Feldmann, F., and Rott, N., "Investigation of Compression Shocks and Boundary Layers in Gases Moving at High Speed," NACA TM-1113, Jan. 1947.

[2]Chapman, D. R., Kuehn, D. M., and Larson, H. K., "Investigation of Separated Flows in Supersonic and Subsonic Streams with Emphasis on the Effect of Transition," NACA TN-3869, March 1957.

[3]Spalart, P., and Strelets, M., "Mechanism of Transition and Heat Transfer in a Separation Bubble," *Journal of Fluid Mechanics*, Vol. 403, 2000, pp. 329–349.

[4]Yang, Z., and Voke, P., "Large-Eddy Simulation of Boundary-Layer Separation and Transition at a Change of Surface Curvature," *Journal of Fluid Mechanics*, Vol. 439, 2001, pp. 305–333.

[5]Balakumar, P., Zhao, H., and Atkins, H., "Stability of Hypersonic Boundary Layers over a Compression Corner," *AIAA Journal*, Vol. 43, No. 4, 2005, pp. 760–767.

[6]Klebanoff, P. S., Tidstrom, K. D., and Sargent, L. M., "The Three-Dimensional Nature of Boundary-Layer Instability," *Annual Review of Fluid Mechanics*, Vol. 12, 1961, pp. 1–35.

[7]Pruett, C. D., Chang, C. L., and Carpenter, M. H., "Spatial Direct Numerical Simulation of High-Speed Boundary-Layer Flows, Part I: Algorithm Considerations and Validation," *Theoretical Computational Fluid Dynamics*, Vol. 7, July 1995, pp. 49–76.

[8]Pruett, C. D., and Chang, C. L., "Spatial Direct Numerical Simulation of High-Speed Boundary-Layer Flows, Part II: Transition on a Cone in Mach 8 Flow," *Theoretical Computational Fluid Dynamics*, Vol. 7, July 1995, pp. 397–424.

[9]Shu, C. W., "Essentially Non-Oscillatory and Weighted Essentially Non-Oscillatory Schemes for Hyperbolic Conservation Laws," NASA CR-97-206253 and ICASE Rept. 97–65, Nov. 1997.

[10]Atkins, H. L., "High-Order ENO Methods for the Unsteady Compressible Navier–Stokes Equations," AIAA Paper 91-1557, June 1991.

K. Ghia
Associate Editor